Geoscience Letters

RESEARCH LETTER

Open Access

Distribution and trend of explosive cyclones over the Southern Ocean and associated atmospheric and oceanic changes during 1980–2020

Xiaoqi Xu[1,2], Jiping Liu[3*], Gang Huang[1,2] and Yifan Ding[4]

Abstract

In this study, we investigate the climatology and trend of explosive cyclones (ECs) over the Southern Ocean (50°S–70°S) during 1980–2020 by combining a method that is most suited for identifying and tracking cyclones in the Southern Ocean and a latest climate reanalysis. On average, approximately 50 ECs are generated annually over the Southern Ocean, with a significant increasing trend of 2.3 per decade during the studying period. This increasing trend is dominated by the trend of strong ECs, particularly in autumn. We analyze the dynamical and thermodynamical effects associated with multiple deepened strong ECs in autumn over an identified key region in the southern Pacific Ocean sector (155°W–170°W, 50°S–65°S), where the density of the initiation of ECs shows the largest increasing trend in autumn. The composite analysis reveals the general patterns and duration of the effects on the atmosphere, ocean, and sea ice associated with multiple ECs in the southern Pacific Ocean. The results indicate that the deepened strong ECs are associated with significant changes in meridional winds, downward longwave radiation, and sensible and latent heat fluxes. These changes lead to cold sea surface temperature anomalies in the northeast of the key region, reaching a maximum 5–7 days after the EC deepening, and the increased sea ice cover south of the key region, peaking 4–5 days after the EC deepening.

Highlights

- Explosive cyclones (ECs) over the Southern Ocean (50°S–70°S) have a significant increasing trend of 2.3 per decade during 1980–2020.
- The increasing trend is dominated by the trend of strong ECs, especially in autumn.
- The anomalies of sea surface temperature and sea ice cover can sustain about 2 weeks following the generation of strong ECs.

Keywords Explosive cyclones, Deepening rate, The Southern Ocean, Sea surface temperature

*Correspondence:
Jiping Liu
liujp63@mail.sysu.edu.cn
Full list of author information is available at the end of the article

Introduction

Explosive cyclones (ECs), also called meteorological "bombs", feature rapid reduction in central pressure, large increase in intensity associated with the Laplacian of central pressure, and often long-lasting relative to ordinary extratropical cyclones (Sanders et al. 1980; Lim and Simmonds 2002; Reale et al. 2019). These severe storms are mainly developed in the mid-to-high latitude oceans. The Southern Ocean is considered as the home to ECs, which largely develop in the Atlantic and Pacific sectors (Sinclair 1995; Allen et al. 2010). Most of ECs typically follow a south-eastward trajectory, undergoing net cyclogenesis in the mid-latitudes and net cyclolysis closer to the Antarctic continent (Reale et al. 2019). They are the synoptic systems derived from baroclinic wave that contribute to transports of energy, momentum, and moisture, influencing surface energy budget, ocean and sea ice states (Raible et al. 2005; Bengtsson et al. 2009). ECs are associated with meteorological hazards, including strong winds (Ashley and Black 2008), heavy precipitation (Pfahl and Wernli 2012; Catto et al. 2015), coastal storm surges (Colle et al. 2008), and sea ice decline (Vichi et al. 2019; Jena et al. 2022).

With the application of automated cyclone tracking schemes and improved quality of atmospheric reanalysis data, analysis of ECs has become possible (Sinclair 1994, 1995; Lim and Simmonds 2002). The EC was first measured by the deepening rate (called Bergeron number), which is defined as the central pressure drop of the cyclone in 24-h interval (Sanders and Gyakum 1980; hereinafter referred to as SG80). To remove the spatial changes of background pressure along the cyclone track, Lim and Simmonds (2002; hereinafter referred to as LS02) modified SG80 by replacing the central pressure with the relative central pressure, the difference between the central pressure of the cyclone and the climatological pressure at that location. To date, LS02 is commonly used but not the only criterion. The choices of the time interval (Yoshida and Asuma 2004; Reale et al. 2019) and the geostrophic adjustment latitude in the equation of deepening rate can be different (Roebber 1984; Gyakum et al. 1989; Fu et al. 2023). Some studies have analyzed climatology and variability of ECs in the Southern Hemispheres using various reanalysis datasets. Using the National Centers for Environmental Prediction (NCEP) reanalysis 2 data, they showed that annual mean frequency of ECs is about 26 per year in the Southern Hemisphere during 1979–1999. Allen et al. (2010) conducted a climatology analysis of ECs during 1979–2008 using four reanalysis datasets. For the European Centre for Medium-Range Weather Forecasts Reanalysis-Interim (ERA-Interim) reanalysis, the number of annual mean ECs in the Southern Hemisphere is about 171 and 53.5 when used the definitions of SG80 and LS02, respectively. Reale et al. (2019) also applied the definition of SG80 to the ERA-Interim reanalysis and showed that 187 ECs occurred per year in the Southern Hemisphere, representing 11% of the total cyclone number in the Southern Hemisphere during 1979–2008. A few studies have examined trends of the frequency of annual mean ECs in the Southern Hemisphere. Lim and Simmonds (2002) found an increase of 0.56 ECs per year during 1979–1999, while Reale et al. (2019) obtained an increase of 0.4 ECs per year during 1979–2008. Reboita et al. (2015) also showed an increase of strong extratropical cyclones during 1979–2012.

While ECs have attracted more attention in recent years, there are limited studies focusing on their variability, such as annual and seasonal climatology and trend (Reale et al. 2019), as well as their characteristics in future scenarios (Reboita et al. 2021). There are few available studies about ECs, and more focuses are on the regions where ECs generate rather than where ECs deepen rapidly. The deepening period of ECs is more important for heat and energy exchanges between the atmosphere and ocean and potential influences. In addition, most of these studies focus on the impact of a specific EC event (Morris and Smith 2001; Vichi et al. 2019; Jena et al. 2022). Thus, the impacts of a series of ECs on atmospheric circulation, ocean and sea ice passing the same region during the deepening period ECs remain unclear.

In this study, we investigate the climatology and trend of ECs over the Southern Ocean for the period 19,802,020 using the latest climate reanalysis from the perspective of generation and deepening period of ECs, considering strong and weak ECs separately. We further explore the cumulative changes of atmospheric circulation (not only as a result but also a generator of ECs), sea surface temperature, and sea ice associated with the occurrence of strong ECs in the typical region where the ECs are prone to deepen.

Data and methods

Data

Six-hourly atmospheric data including sea level pressure (SLP), near surface air temperature and winds, sensible and latent heat fluxes, shortwave and longwave radiations, and total cloud cover during 1980–2020 are obtained from the 5th generation European Centre for Medium-Range Weather Forecasts (ECMWF) reanalysis with a spatial resolution of $0.25^\circ \times 0.25^\circ$ (ERA5; Hersbach et al. 2023). The ERA5 reanalysis is based on the global Numerical Weather Prediction Model Integrated Forecast System (IFS) Cy41r2, benefiting from a decade of developments in model physics, core dynamics, and data assimilation. It shows an improved fit for pressure, temperature, humidity, and winds in the troposphere when

compared with ERA-Interim. (Hersbach et al. 2020). The daily sea ice concentration data re obtained from the National Snow and Ice Data Center (NSIDC) Climate Data Record of Passive Microwave Sea Ice Concentration (Version 4) with a spatial resolution of 25 km × 25 km (NSIDC CDR; Meier et al. 2021). The daily sea ice motion data are from the Polar Pathfinder Sea Ice Motion Vectors dataset (version 4), which are provided daily from 1979 onward by NSIDC at 25 km resolution (Tschudi et al. 2019). The daily sea surface temperature data are obtained from the National Oceanic and Atmospheric Administration Daily Optimum Interpolation Dataset Version 2.1 with a spatial resolution of 0.25° × 0.25° (OISST v2.1; Huang et al. 2020), which is a blended objective analysis of both in situ measurements and satellite observations.

Methods

Cyclone detection and tracking algorithm

Several cyclone detection and tracking algorithms have been developed (e.g., Neu et al. 2013; Grieger et al. 2018). The question is which one is most suited for identifying and tracking cyclones in the Southern Ocean. Grieger et al. (2018) compared consistency and discrepancy of cyclones in the sub-Antarctic region obtained from 14 methods using the ERA-Interim atmospheric reanalysis during 1979–2008. Their results suggested that among the 14 methods analyzed, the method developed by Serreze et al. (1995, 2008) shows cyclone characteristics that are closer to the average of the multiple methods. In this study, we use an improved version of this cyclone detection and tracking algorithm, which was introduced by Crawford and Serreze (2016). One problem with simple SLP-based methods in Serreze (1995) is unrealistic splitting of cyclone tracks into multiple parts. In the improved algorithm, the track of a cyclone with multiple centers will continue if any of its centers persists. That means it can identify multi-center cyclones, to avoid wrongly identifying the subcenter of a cyclone as another single cyclone. In detail, this algorithm identifies cyclones using minimum SLP. The main approach is to search through every grid cell in the input SLP field and identify grid cells that have a lower pressure than their eight neighboring grids. It is a Lagrangian method, focusing on the development of features as they move through space, which can give more information about individual cyclones than Eulerian method. It has included some features of more recent cyclone identifying and tracking techniques, i.e., explicit detection of multi-center cyclones as well as merging and splitting cyclones (Wernli and Schwierz, 2006;Inatsu 2009; Hanley and Caballero 2012; Crawford and Serreze 2017). It also uses the Equal-Area Scalable Earth 2.0 grid (EASE2) rather than regular longitude–latitude grid, which prevents biases of over-counting cyclone density where grid size becomes smaller (i.e., more SLP minima per million sq. km could be identified, if there are more grid cells within those million sq. km). The EASE2 grid also has relatively small errors in distance/angle in the Antarctic (see Crawford and Serreze 2016, 2017 for details). Here the 6-hourly ERA5 SLP fields are projected on the Southern Hemisphere EASE2 grid with a grid cell size of 100 km by 100 km (Brodzik et al. 2012), which is based on a Lambert's equal-area azimuthal projection. We defined the Southern Ocean as the ocean between 50 and 70°S.

Definition of ECs

The EC is defined by relative normalized deepening rate following Sanders and Gyakum (1980) and Lim and Simmonds (2002). The relative normalized deepening rate ([NDR]r) is calculated using the equation below:

$$[NDR]_r = \frac{\Delta P_r}{24} \cdot \frac{sin60}{sin|\varnothing|} \quad (1)$$

where ΔPr is the variation of relative central pressure over a period of 24-h, centered around the time when the cyclone occurs, and ϕ is the mean latitude during that period, and r means the relative central pressure. The relative central pressure is computed as the anomaly with respect to the 6-hourly ERA5 SLP climatology at each grid point, which eliminates the change in background pressure as the cyclone moves toward higher latitudes. When [NDR]r of the cyclone is larger than 1, it is classified as an EC.

The EC's cyclogenesis is defined as the first appearance of an EC and the deepened ECs is defined as the appearance when the cyclone fulfills the criterion of the EC. That means we found the location where it first satisfies the criterion [NDR]r > = 1 during the cyclone period, and then counted it as 1. Both the EC's cyclogenesis and deepened ECs are mapped as cyclone track density, which is the number of cyclone tracks occurring per time interval per unit area (500 km^2) and every cyclone is counted as 1 rather than many times during the cyclone period. Hereafter, they are referred to as density of the cyclogenesis of ECs and density of the initiation ([NDR] r > = 1) of ECs.

We further divide the EC detected as above into two groups (strong and weak) based on lifetime maximum cyclone intensity. The intensity for a single cyclone at each time interval is quantified by computing the Laplacian of the mean SLP field ($\nabla^2 P$) over the grid point where cyclone center is located. Following Lim and Simmonds (2002), here cyclones with a $\nabla^2 P$ value greater than 0.7 $hPa/10^4 km^2$ are classified as strong ECs and the

others with the value less than that value are classified as weak ECs.

Results

Climatology and trend of ECs

We count the total number of ECs generated in the Southern Ocean (50°S–70°S) for each individual year during 1980–2020. As shown in Fig. 1a, the number of ECs ranges from 40 to 70 per year, with the average number of 51.7 per year during 1980–2020 (Table S1). There is a significant increasing trend of about 2.3 ECs per decade. It is primarily due to the increase from 1980 to the early 2010s, in part due to large number of strong ECs in 2009 and weak ECs in 2008 and 2010. As described in Sect. "Data and methods", we divide ECs in two categories. It appears that the average number of strong ECs (24.1 per year) is relatively less than that of weak ECs (27.7 per year), largely due to the difference in summer (Table S1). However, these two kinds of ECs have different trends. As shown in Fig. 1b, the occurrence of strong ECs increases significantly by 1.62 per year during 1980–2020, while weak ECs have no significant trend. This implies that the ECs might not only increase but also be more intense in the last 4 decades.

To examine the sensitivity to the threshold for separating the weak and strong ECs, we show the histogram distribution and trends of ECs with different intensities in Fig. S1. The frequency of cyclone intensity between 0.6 and 0.7 is the highest (Fig. S1a). When the shading is in the same side of the zero-line, it means that the trend of ECs is statistically significant at 95% confidence level using a Student's *t* test (Fig. S1b). Based on this, the trend of ECs is positive and significant when the threshold is set to 0.7 or below.

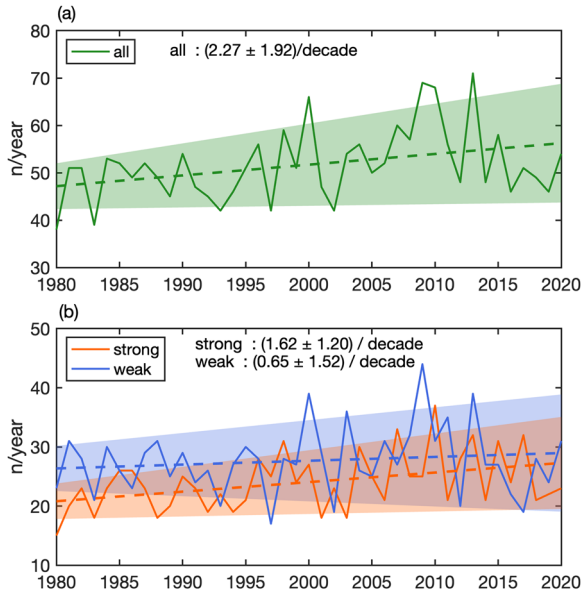

Fig. 1 Time series and linear trends of ECs during 1980–2020. **a** All ECs and **b** strong and weak ECs separately (The shading represents the confidence range for trend coefficient estimates at 95% significance level)

Figure 2a shows the climatology of the density of cyclogenesis of ECs. The ECs preferentially occur in the region extending from the central Indian to southwestern Pacific sectors, with the largest density in the ocean off the coast of Victoria Land and Wilkes Land (up to about 1 track per year per unit area). In addition, the ocean off the coast of south-eastern America and around Antarctic Peninsula are in favor of the EC generation. For strong and weak ECs, both exhibit the similar spatial pattern (Fig. 2b, c). The density of the cyclogenesis of strong ECs is about one third of total ECs over most of the Southern Ocean. Figure 2d shows the trend patterns of total EC density. The largest and significant increasing trend is located in the ocean north of Wilkes Land (~ 130°E-155°E, 50°S-65°S, up to 0.12 per decade). Meanwhile, a significant decreasing trend is observed to the northwest of Ross Sea. This dipole-like spatial distribution corresponds to the region with highest climatological density of the cyclogenesis of ECs, which implies a westward shift of maximum ECs genesis (Fig. 2a). Another significant increasing trend is found in the ocean north of Queen Maud Land (~ 10°E–30°E, 60°S–70°S). The trends of strong and weak ECs are shown in Fig. 2e–f, which are generally consistent with that of the total ECs. The largest and significant increase in the ocean north of Wilkes Land is largely attributed to the significant increase of strong ECs, while the significant increase in the ocean north of Queen Maud Land results from a combination of strong and weak ECs. This suggests that the occurrence of strong ECs becomes more often in the ocean north of Wilkes Land. By contrast, the significant decrease to the west of the Ross Sea is more related to the significant decrease of weak ECs.

Besides, we not only focus on where the ECs generates but where ECs tend to deepen. We further identify the regions that favor ECs deepening. The climatology of the density of the initiation ([NDR] $r >= 1$) of ECs shows that the ECs typically deepen over a zonal band extending from the southern Indian Ocean to the southern Pacific Ocean (Fig. 3a). Both strong and weak ECs show similar distributions though they have different location of maximum values (Fig. 3b, c). The maximum of strong ECs is located in the northeast to the region with the largest density of the cyclogenesis of strong ECs (Figs. 2b, 3b), while the maximum of weak ECs occurs in the north/northwest to the largest density of the cyclogenesis of weak ECs (Fig. 2c, Fig. 3c). The relative position of maximum density of cyclogenesis

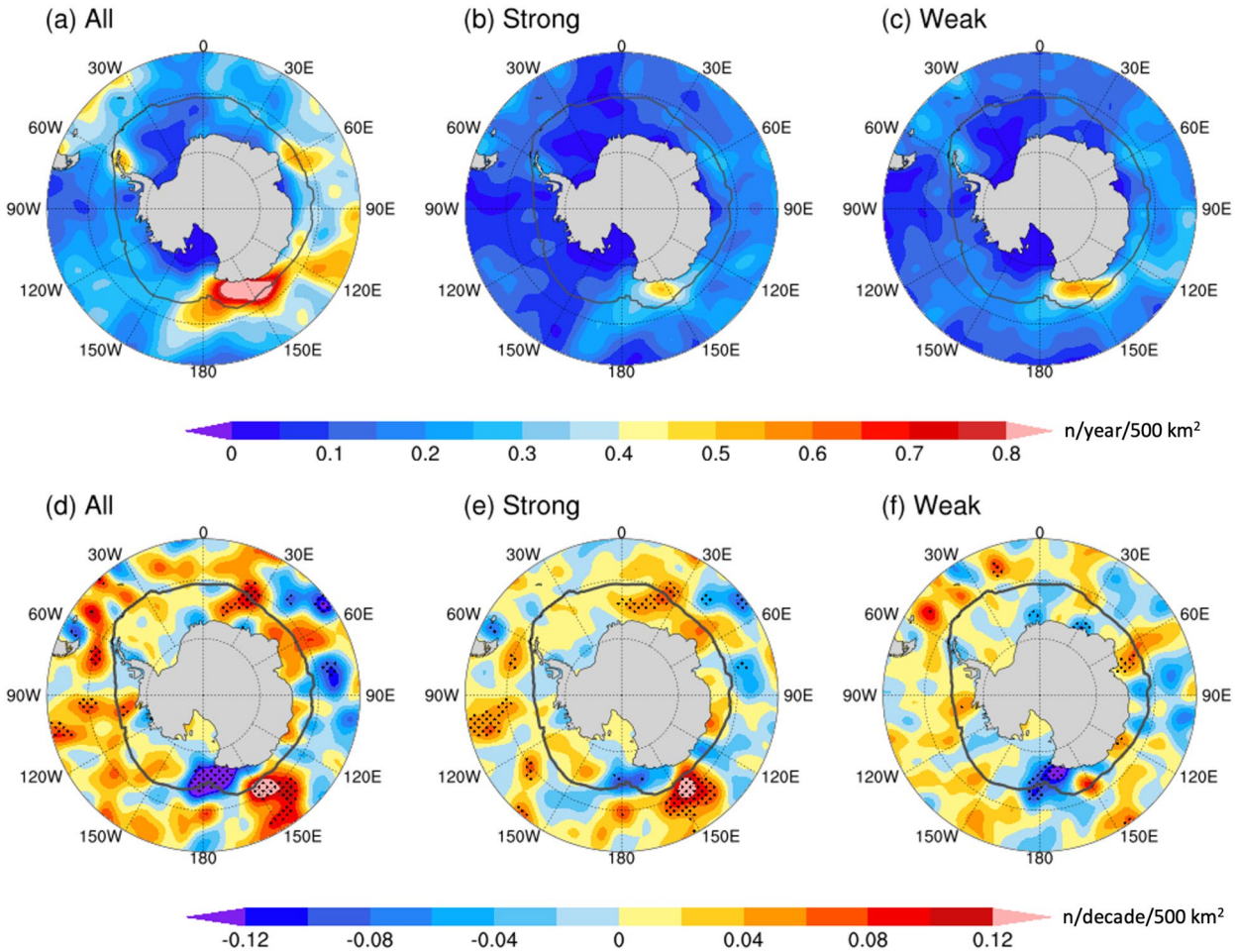

Fig. 2 The climatology of the density of the cyclogenesis of **a** all ECs, **b** strong ECs, and **c** weak ECs. The trend of the density of the cyclogenesis of **d** all ECs, **e** strong ECs, and **f** weak ECs during 1980–2020. (The dotted area is statistically significant at 99% confidence level using a Student's *t* test. The grey line outlines the sea ice edge based on the contour of 15% climatological sea ice concentration during 1980–2020)

and the initiation ([NDR]r ≥ 1) of strong ECs and weak ECs differ. However, according to the composite SLP anomaly fields, 3 days after the ECs are generated (see Fig. S2 and Text S1 for details), both strong and weak ECs develop along an eastward-moving trajectory. This implies that the location of the deepened ECs does not necessarily coincide with their genesis location, as cyclones move during their life cycles. Figure 3d shows the trend pattern of the density of the initiation ([NDR] $r >= 1$) of all ECs. It illustrates a distribution where increasing and decreasing trends are interspersed. In addition, only a few areas with increasing trends are significant, whereas the areas with decreasing trends are generally not significant and smaller (Fig. 3d). The two largest increasing trend centers are located in the ocean north of Wilkes Land, where favor EC generation. The east one (160°E–170°E, 55°S–65°S) is largely associated with the strong ECs, while the west one (120°E–135°E, 50°S–65°S) is attributed to both strong and weak ECs (Fig. 3e–f).

Previous studies suggested that extratropical cyclones have strong seasonality, the winter is the most cyclogenetic season (Hodges et al. 2011; Reboita et al. 2015). Wang et al. (2013) also showed that there are notable seasonal variations in the cyclone's trends. Figure S3a provides the distribution (including the median and quartiles) of the number of ECs in the whole year and each season. As for total ECs, winter is the most active season of explosive cyclogenesis with a relatively large spread-out range (the green boxes in Fig. S3a). According to Table S1, the highest seasonal average of all ECs is observed in winter (17.3 per year), accounting for one third of all seasons, followed by autumn (15.71 per year), spring (11.49 per year), and summer (7.15 per year). The standard deviations in Table S1 indicate the dispersion of the numbers of ECs over the past 4 decades. Figure 4

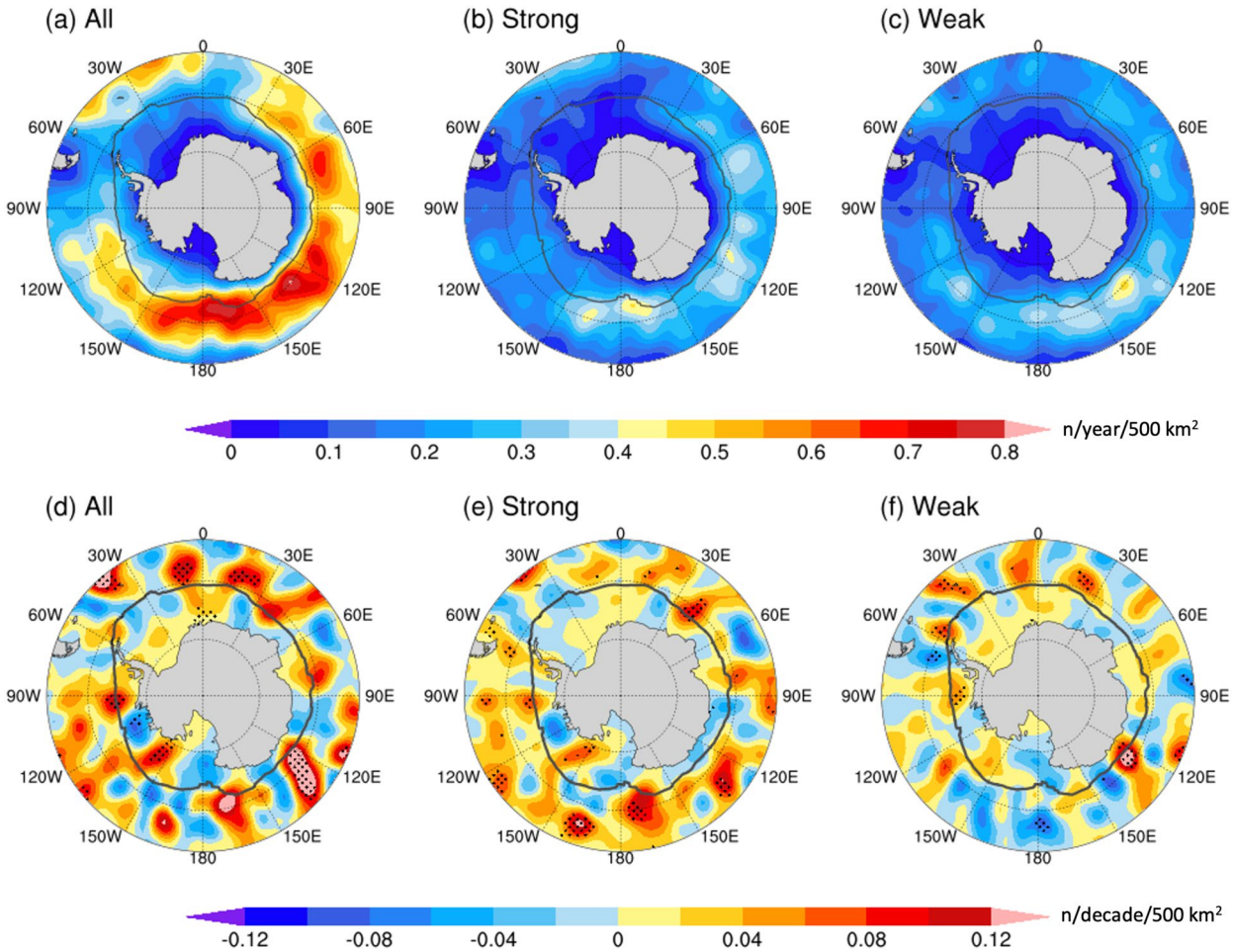

Fig. 3 The climatology of the density of the initiation ([NDR]r > = 1) of **a** all ECs, **b** strong ECs, and **c** weak ECs. The trend of the density of the initiation ([NDR]r > = 1) of **d** all ECs, **e** strong ECs, and **f** weak ECs during 1980–2020. (The dotted area is statistically significant at 99% confidence level using a Student's *t* test. The grey line outlines the sea ice edge based on the contour of 15% climatological sea ice concentration during 1980–2020)

exhibits the trends of ECs numbers in each season. For total ECs, only the trend in autumn is statistically significant (increasing by 1.1 per decade), which account for half of the significant annual trend. As for strong and weak ECs, the seasonal trends of strong ECs (the orange bars in Fig. 4) are similar to those of the total ECs (the green bars in Fig. 4), whereas the weak ECs (the purple bars in Fig. 4) have no significant trends for all seasons. This indicates that the seasonal trends are dominated by strong ECs, especially in autumn. In addition, the annual and seasonal statistics of EC features, including cyclone lifetime and deepening period (see the definition in Text S2), are shown in the supplement (see Figs. S3–S4; Text S3 for more details).

The analysis above concludes that strong ECs have the highest and significant increasing trend in autumn (Fig. 4). Since we aim to focus on the region where the ECs are prone to deepen, our further investigation is on the trend field of deepened ECs in autumn. As shown in Fig. 5, the seasonal trend of the density of the initiation ([NDR] $r >= 1$) of strong ECs in autumn exhibits similar features as that of annual strong ECs (Fig. 3e). There is a significant increasing trend located north to the Ross Ice Shelf, with the value up to 0.1 per decade. This key region (155°W–170°W, 50°S–65°S) has the largest and significant trend of the density of the initiation ([NDR] $r >= 1$) of strong ECs and is located near the largest density of the cyclogenesis of strong ECs, following the eastward-moving trajectory of cyclones.

The rapid decrease of the central pressure during the period of deepened strong ECs must be associated with large variation in atmospheric circulation. This finally influences the changes of sea surface and sea ice by dynamic and thermodynamic processes. Compared to climatology, we are more interested in trends, as trends better reflect the changes over the past 4 decades. In

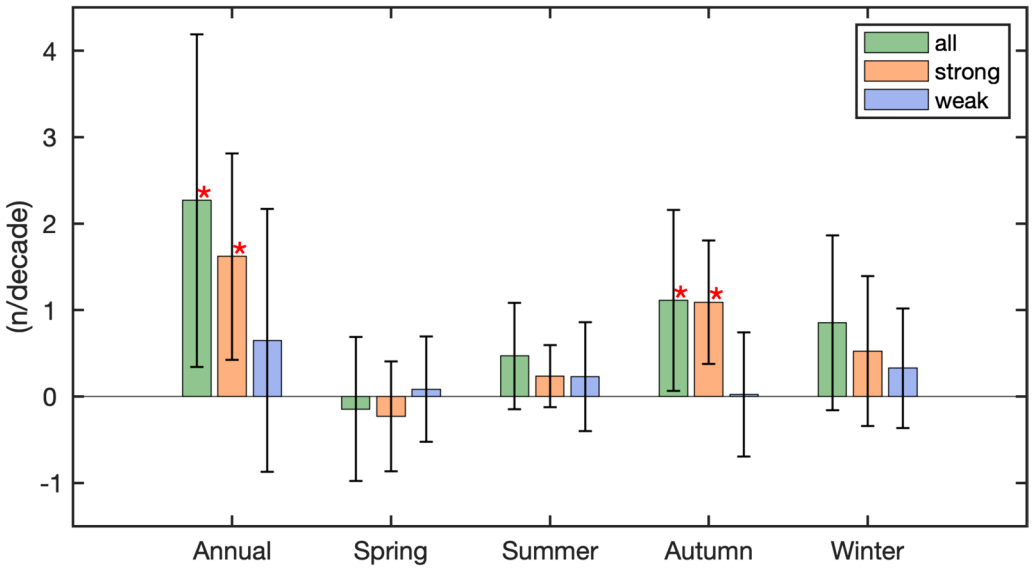

Fig. 4 The annual and seasonal trends of the numbers of all ECs (green bars), strong ECs (orange bars), and weak ECs (purple bars). The red stars highlight the significance at 95% confidence level using a Student's *t* test

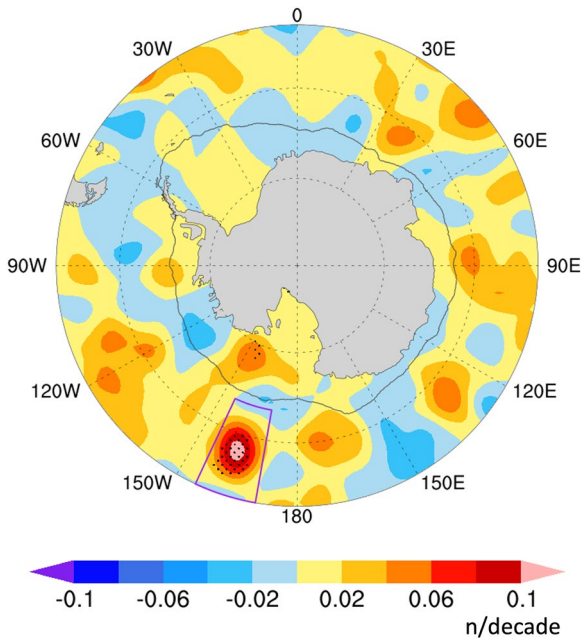

Fig. 5 Spatial distribution of the trend for deepening of strong ECs in autumn. (The dotted area is statistically significant at 99% confidence level using a Student's *t* test. The grey line outlines the sea ice edge based on the contour of 15% climatological sea ice concentration during 1980–2020. The purple box indicates the key region (155°W–170°W, 50°S–65.°S) which has the largest and significant increasing trend of deepening ECs in autumn)

addition, we focus on where ECs tend to deepen rather than where they generate. Considering these two points, we select the key region with the highest and most significant increasing trend of deepened ECs in autumn (purple box in Fig. 5) to analyze changes in atmospheric states, as well as ocean and sea ice, during the period of deepened ECs.

Changes in atmospheric and oceanic states associated with ECs in the focused region

There are 34 cases that met the criterion for EC when they passed through the purple box (the region with the largest and significant increasing trend of deepening ECs). To analyze changes of atmospheric conditions associated with ECs at synoptic scale, we select the time when [NDR]r reached the threshold of EC in the purple box (Fig. 5) and the subsequent 3 days for each case to generate the composite anomalies field by subtracting the climatology in autumn of essential atmospheric variables. As shown in Fig. 6a, a strong cyclonic circulation is located in the southern Pacific Ocean sector (~170°W–110°W, 50°S–70°S), with the largest pressure anomaly to 16 hPa, which is in line with the closed low height center at 500 hPa. There are large northward wind speed anomalies to the west of the composite low-pressure anomaly center (Fig. 6b). Thus, ECs observed at the purple box are associated with strong advection of cold air from the Ross Ice Shelf into the Southern Ocean, leading to a cooling of up to 3 °C extending from ice-covered coastal Ross Sea to the south of New Zealand (Fig. 6c). The total cloud cover shows an out-of-phase anomalies between the area in the northwest of the box and the region in the east of the box. Such characteristics display the mature stage of cloud vortex with spiraling of clear air

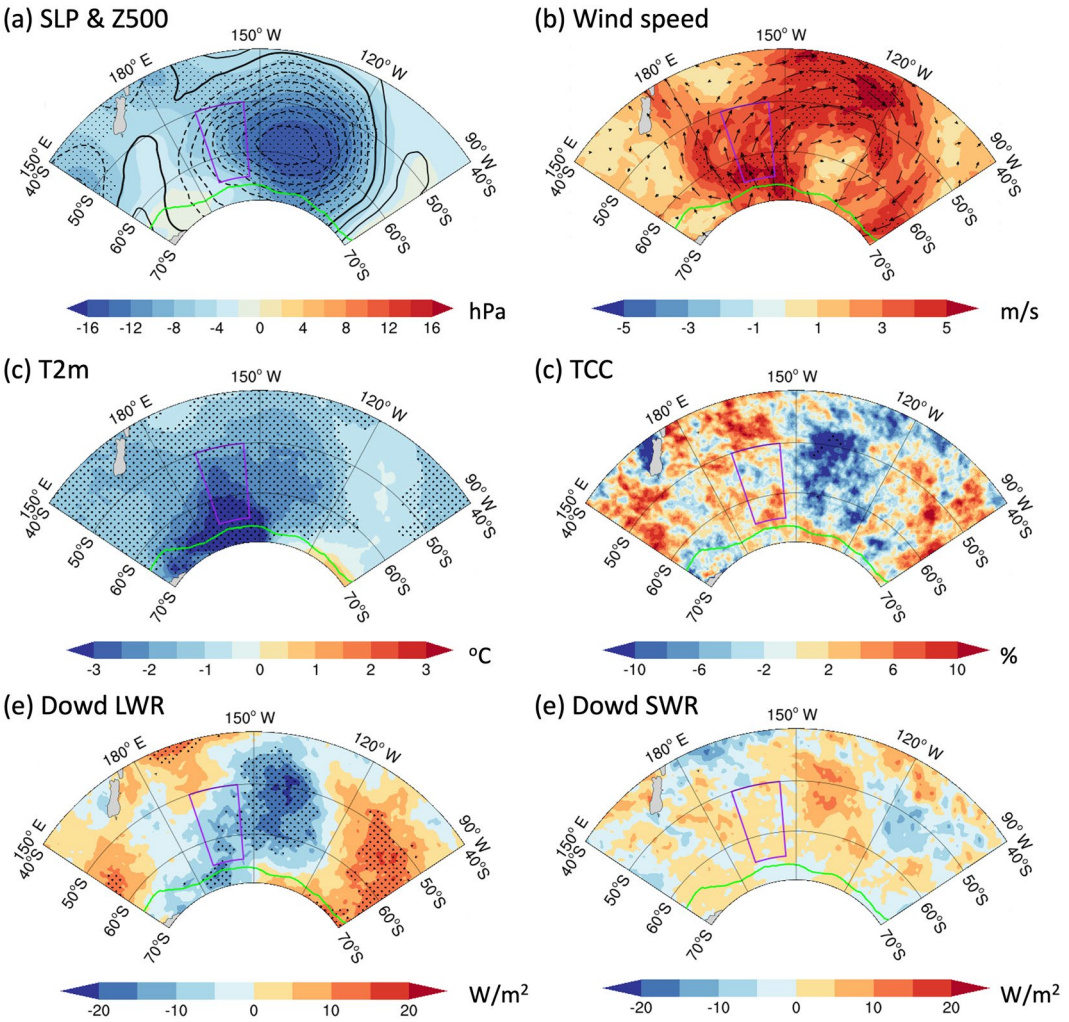

Fig. 6 The composite anomaly fields for 34 cases in autumn of atmospheric parameters for 3 days since the strong ECs deepened at the purple box: **a** sea level pressure (shaded) and geopotential height at 500 hPa (contour; the interval is 2 hPa); **b** wind speed at 10 m (shaded) and wind vectors (arrows); **c** temperature at 2 m; **d** total cloud cover; **e** downward longwave radiation and **f** downward shortwave radiation (The dotted area is statistically significant at 95% confidence level using a Student's *t* test. The green line outlines the sea ice edge based on the contour of 15% climatological sea ice concentration in autumn during 1980–2020. The purple box indicates the key region (155°W–170°W, 50°S–65.°S) which has the largest and significant increasing trend of deepened ECs in autumn)

around a well definite center (Fig. 6d) (Streten and Troup 1973; Carleton and Carpenter 1990). The distribution of downward longwave radiation anomalies conforms to changes in total cloud cover (Fig. 6e). Significant positive (negative) downward longwave radiation anomaly occurs in the area in the northwest of the box and the area in the east of the box. The downward shortwave radiation anomalies have opposite sign to changes of total cloud cover, but the anomalies are not significant (Fig. 6f). The large-scale circulation pattern in Fig. 6 implies meridional heat transport to the east of the composite low-pressure center. It implies that some ECs are likely to coincide with intense Atmospheric Rivers (ARs), which acts as a narrow channel of moisture flux from low latitudes to high latitude (Gorodetskaya et al. 2014; Wille et al. 2021). One EC case study about the feature of AR is shown in the supplement (see Fig. S5 and Text S4–S5 for more details).

The deepened ECs can also influence the changes of air–sea heat fluxes. As shown in Fig. 7a, the significant negative net heat flux anomalies, with the highest values up to 80 W/m^{-2}, occurs around the composite cyclone center and the region east of it. This means that the ocean releases heat energy to the atmosphere where the cyclones deepen to the EC's threshold. This upward net heat flux anomaly is mainly due to three contributors:

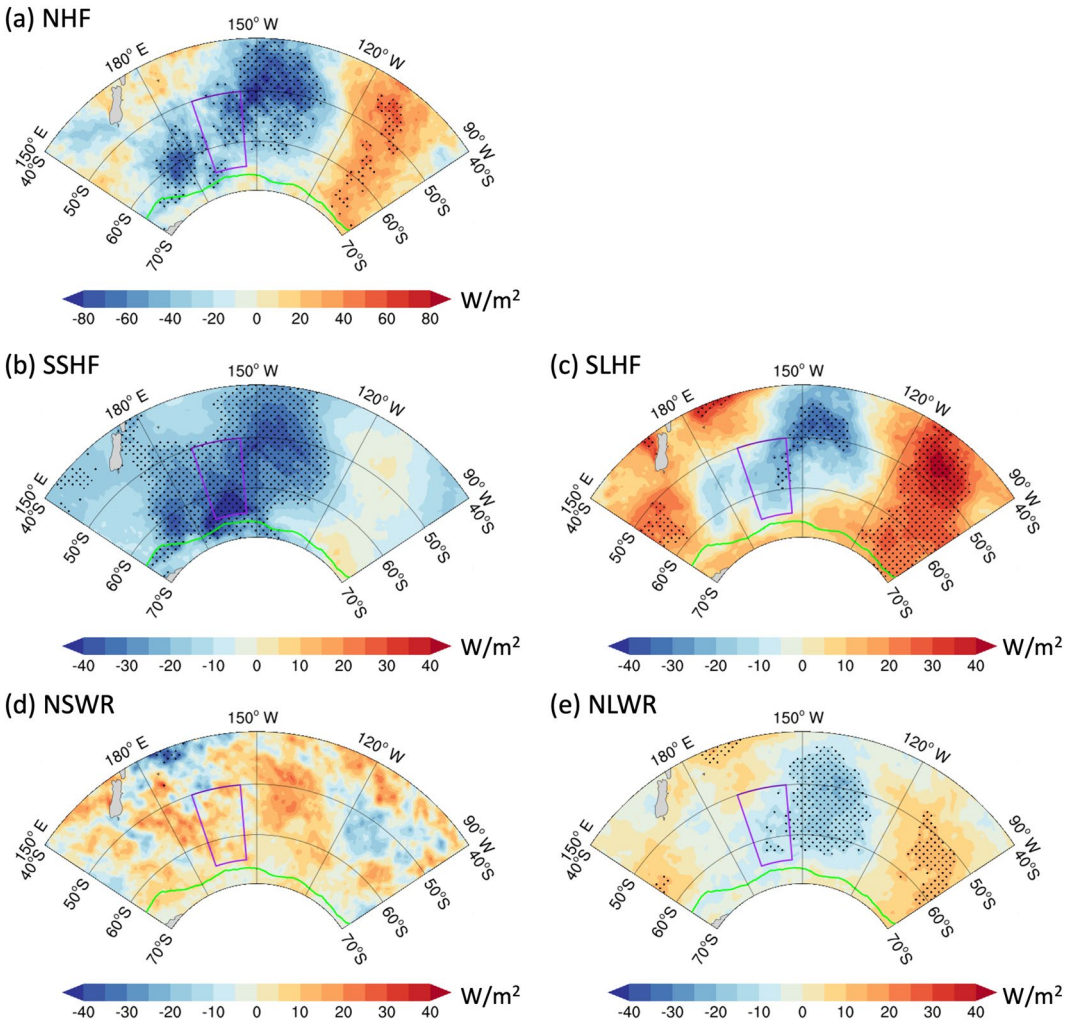

Fig. 7 The composite anomaly fields for 34 cases in autumn of heat fluxes for 3 days since the strong ECs deepened at the purple box: **a** net heat flux; **b** surface sensible heat flux; **c** surface latent heat flux; **d** net shortwave radiation, and **e** net longwave radiation. (The positive values of radiation and heat flux mean the downward direction from atmosphere to ocean. The dotted area is statistically significant at 95% confidence level using a Student's *t* test. The green line outlines the sea ice edge based on the contour of 15% climatological sea ice concentration in autumn during 1980–2020. The purple box indicates the key region (155°W–170°W, 50°S–65°S) which has the largest and significant increasing trend of deepened ECs in autumn)

sensible heat flux, latent heat flux, and net longwave radiation over sea surface. Around the composite low-pressure center, the strong offshore winds carry cold air northward, increasing the temperature difference, which favors the upward sensible heat flux (Fig. 7b). The intensified wind speed enhances evaporation and further releases more latent heat flux from the ocean to the atmosphere (Fig. 7c). Meanwhile, this region is located in the clear area of cloud vortex, which decreases net longwave radiation (Fig. 6d). In addition, the significant positive net heat flux anomalies are found over the east side of the composite low-pressure center. This is mainly attributed to the increase of net longwave radiation and latent heat flux which are associated with increase of cloud cover and reduced wind speed in that area. Thus, the significant release of heat fluxes from the ocean to the atmosphere implies that the underlying sea surface would be colder during the deepening period of ECs.

In addition, we derived the composite fields of sea surface temperature (SST) and sea ice concentration (SIC), which can partly reflect the impacts of the ECs. Figure 8a, b shows the averaged changes of sea surface temperature (SST) and sea ice concentration (SIC) during a 3-day period since the ECs deepened at the purple box. The widespread SST cooling occurs in the northeast of the purple box, with the largest anomaly value up to 0.16 °C.

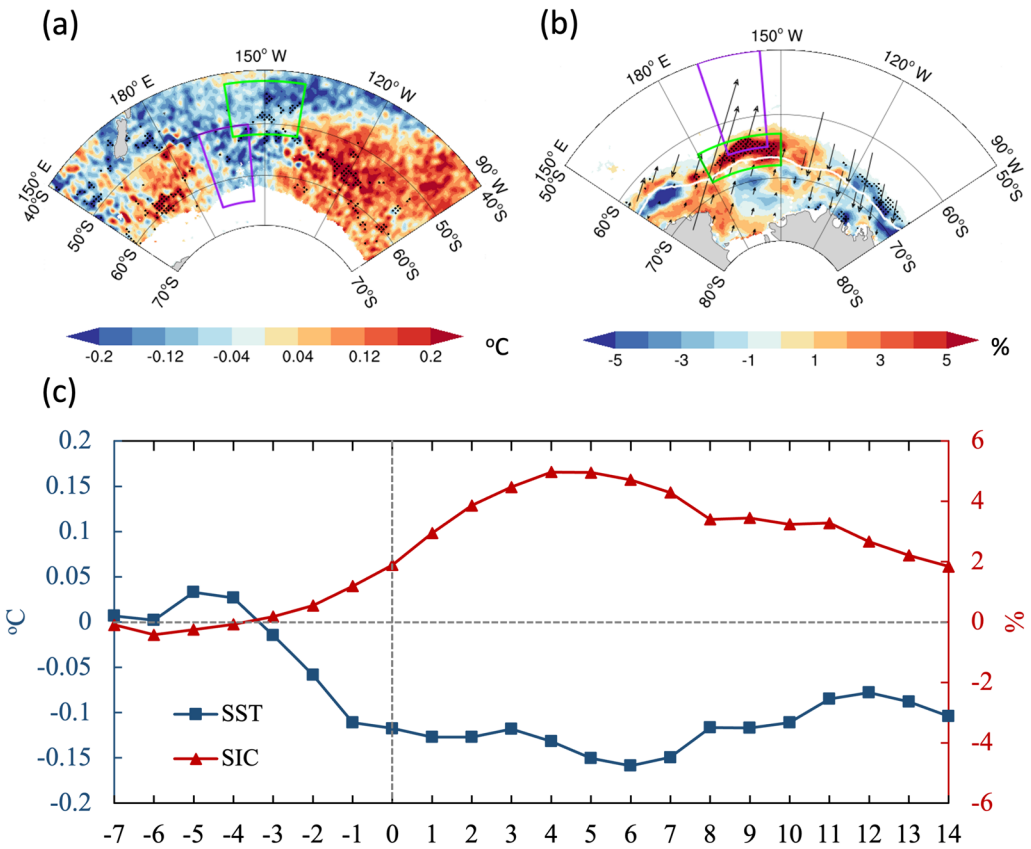

Fig. 8 The composite anomaly fields for 34 cases in autumn of **a** sea surface temperature (SST) and **b** sea ice concentration (SIC) for 3 days since the strong ECs deepened in the purple box (The arrows indicate the sea ice movement. The dotted area is statistically significant at 95% confidence level using a Student's *t* test. The white line outlines the sea ice edge based on the contour of 15% climatological sea ice concentration during 1980–2020). (**c**) Time series of area-averaged SST and SIC in the green box in Fig. 8a–b within a 1-week prior period and a 2-week lag period since the strong ECs deepened in the purple box at time 0

Then the region with the widespread SST cooling was chosen to investigate the duration of the potential effects. The negative anomaly of SST and positive anomaly of SIC occur 3 or 2 days before the categorization as EC, since the cyclone is developing and strengthening near there. After that, the SST cooling enhances and reaches the maximum anomaly on the day 5–7, and then reduces to a smaller anomaly (the blue line in Fig. 8c). In general, SST cooling anomaly occurs at the north-eastern side of ECs deepened region (40°S–50°S, 140°W–160°W) 3 days later, though the amplitudes are various. As shown in Fig. S6, the cooling anomaly induced by EC could extend to wider region (40°S–50°S, 120°W–160°W) with the anomaly of about -1 °C in some cases like case 2 (cyclogenesis time: 1984/04/02) and case 12 (cyclogenesis time: 1998/03/15), while some were relatively weak, like for instance case 3 (cyclogenesis time: 1986/04/16) and case 11 (cyclogenesis time: 1996/05/01). For example, the SST shows warming anomaly in the focused region in case 15 (cyclogenesis time: 2003/04/03) and case 16 (cyclogenesis time: 2004/04/17). The SST change is attributed to both dynamic and thermodynamic processes. Regarding the distribution of the composite field (Fig. 8a), the SST cooling is located in the northeast of the strongest northward wind anomalies (140°W-160°W, 45°S-55°S; Fig. 6b). It is also consistent with the negative net heat flux anomaly (Fig. 7a), indicating that the ocean loses heat to the atmosphere as the ECs deepen. Meanwhile, the SST warming occurs near sea ice edge at around 180°E and 120°W, the latter is in part due to positive net heat flux there. The ocean mixing associated with the strong surface wind might be also contributed to this warming. As for SIC, it increases by about 5% at the margin (the green box in Fig. 8b; 63°S–68°S, 180°E–150°W) on the west side of the composite low-pressure center (Fig. 6a) and decreases by approximately 3% on the east side. This variation appears to be related to the offshore and onshore winds driving sea ice movement as ECs pass. However, this result is derived from a composite field, and thus only reflects the possible distribution of anomalies that

may occur when ECs deepen in this area. This increase of SIC in the green box reaches the maximum at day 4–5 after the deepening of strong ECs and gradually decrease (the red line in Fig. 8c).

Discussion and conclusion

In this study, we analyze the climatology and trend of ECs over the Southern Ocean for the period 1980–2020 by combining the latest climate reanalysis data and a method which is more suited for identifying and tracking cyclones in the mid-to-high latitudes. Typically, there are 51.7 ECs generated annually over the Southern Ocean and about half of them are strong ECs. About 65% of ECs occur during the cold season, which is roughly consistent with the result for the entire Southern Hemisphere (Reale et al. 2019). The high-density area of cyclogenesis of ECs is observed in the central Indian to southwestern Pacific sectors of the Southern Ocean, while a zonal band from the southern Indian Ocean to the southern Pacific Ocean shows high frequency of ECs deepening.

A significant increasing trend of ECs is found in the Southern Ocean during 1980–2020 (about 2.3 per decade). Some studies have reported the increase of ECs for the entire Southern Hemisphere using shorter data records (Lim and Simmonds 2002; Reboita et al. 2015; Reale et al. 2019). Importantly, we show that the increase of ECs in the Southern Ocean is dominated by the trend of strong ECs, suggesting that ECs might not only increase but also be more intense in recent decades. The seasonal trends are also dominated by strong ECs, especially in autumn. The most significant increase of explosive cyclogenesis is located at the ocean north of Wilkes Land, and the region with the largest increase of the deepened strong ECs is located in the southern Pacific Ocean sector. It seems that the strong ECs are not only prone to generate over the ocean north of Wilkes Land but tend to strengthen and deepen over there. Previous studies indicated that Southern Annular Mode (SAM) was originally thought to characterize meridional shifts in the storm track across the southern hemisphere (Spensberger et al. 2020). Fogt and Marshall (2019) investigated seasonal means of the three main types of SAM indices and suggested that the significant positive SAM trends during 1979–2018 were observed mostly in austral summer and autumn. The intensified SAM in autumn would enhance the westerly winds and modify the storm tracks, which partly explains the increasing trend of ECs in autumn. But it is an open question, requiring further studies to reveal the causes of seasonal variabilities of ECs trends over the Southern Ocean.

Based on case studies, some researchers have examined characteristics of EC in the Southern Ocean and their associated changes (Reale et al. 2019; Reboita et al. 2021). However, little is known about the accumulated impacts of ECs in the Southern Ocean on atmosphere, ocean, and sea ice. Here we select a key region in the south-eastern Pacific that has a significant increasing trend of strong ECs deepening in autumn to investigate the composite effects. Our composite analyses show that the multiple deepened strong ECs are associated with the cyclonic surface winds, warm and moist air flux to the east of the EC core, and cold and dry air flux to the west over the Southern Ocean, although the magnitudes might differ (not show). These corresponding features reveal the general patterns of the effects induced by multiple ECs in a selected region, but the total effects of ECs on the entire Southern Ocean need further study.

Previous studies focused on the rapid response of sea surface and sea ice to specific ECs and pay more attention to the duration of their atmospheric characteristics rather than the persistence and recovery of the sea surface temperature and sea ice cover anomalies after the deepening of ECs (Vichi et al. 2020; Turner et al. 2020; Jena et al. 2022). These studies displayed the evolution of a single EC over 3–4 days. Similarly, we derive the evolution during and after the deepening period for the composite fields. It shows that sea surface cooling anomalies in the northeast of the key region begin to enhance 3 days before the EC deepening (day 0) and reach a maximum 5–7 days after the EC deepening, and the increased sea ice cover south of the key region reaches the maximum at day 4–5 after EC deepening. The overall impact of cyclones on the sea ice changes is complex. We just showed the composite effect of ECs on SIC in particular region. The role of total ECs in variability of Antarctic Sea ice conditions remained uncertain. Several studies have proposed some approaches to investigate the impacts of cyclone on the Arctic sea ice (Schreiber and Serreze 2020; Finocchio et al. 2020). For example, Finocchio et al. 2020 used a new metric called the cross-ice-edge wind and quantified its relationship to subsequent changes in sea ice extent around cyclones. Some studies distinguished the relative importance of the dynamic and thermodynamic processes of Arctic cyclones on sea ice using sea ice modeling (Clancy et al. 2021). These approaches can be also applied in the analysis of Antarctic sea ice in the future study.

The composite analyses in this study reveal the spatial distributions and amplitude of the impacts of strong ECs on surrounding environment but also include the effect of the large-scale atmospheric circulation. In addition, the atmosphere–ocean–sea ice interactions during strong ECs which are associated with complex, nonlinear mechanisms remain unclear. To distinguish the role of synoptic-scale system and large-scale field, and quantify

the contributions of detailed physical processes, further numerical modelling studies are needed.

Abbreviations

ECs	Explosive cyclones
SG80	The automated cyclone tracking schemes proposed by Sanders and Gyakum (1980)
LS02	The automated cyclone tracking schemes proposed by Lim and Simmonds (2002)
NCEP	National Centers for Environmental Prediction
ERA-Interim	European Centre for Medium-Range Weather Forecasts Reanalysis-Interim
SLP	Sea level pressure
ECMWF	European Centre for Medium-Range Weather Forecasts
ERA5	The 5th generation European Centre for Medium-Range Weather Forecasts Reanalysis
IFS	Integrated forecast system
NSIDC	National Snow and Ice Data Center
OISST v2.1	The National Oceanic and Atmospheric Administration Daily Optimum Interpolation Dataset Version 2.1
EASE2	Equal-Area Scalable Earth 2.0 grid
[NDR]r	The relative normalized deepening rate

Supplementary Information

The online version contains supplementary material available at https://doi.org/10.1186/s40562-024-00356-4.

Supplementary file 1.

Acknowledgements
The authors are sincerely grateful to the anonymous reviewers and the editor for their constructive comments on this paper.

Author contributions
X. Q. Xu contributed to data analyses and wrote the manuscript; J. P. Liu supervised the research and provided the idea and revised the manuscript; G. Huang gave some suggestions; Y. F. Ding gave some technical supports. All authors read and approved the final manuscript.

Funding
This research was supported by the Southern Marine Science and Engineering Guangdong Laboratory (Zhuhai) (Nos. SML2023SP219 and SML2023SP217) and the National Key Scientific and Technological Infrastructure project "Earth System Science Numerical Simulator Facility" (Earth Lab).

Availability of data and materials
All the data analyzed here are openly available. The National Oceanic and Atmospheric Administration Daily Optimum Interpolation dataset Version 2.1 is available at https://doi.org/https://doi.org/10.25921/RE9P-PT57. The National Snow and Ice Data Center (NSIDC) Climate Data Record of Passive Microwave Sea Ice Concentration (Version 4) is obtained at https://nsidc.org/data/g02202/versions/4. Polar Pathfinder Daily 25 km EASE-Grid Sea Ice Motion Vectors (Version 4) is obtained at https://nsidc.org/data/nsidc-0116/versions/4. ERA5 hourly data on single level is provided by Copernicus Climate Change Service (C3S) Climate Data Store (CDS) (Accessed on 01-02-2021) https://doi.org/10.24381/cds.adbb2d47 at https://doi.org/https://doi.org/10.24381/cds.adbb2d4. The satellite cloud images are obtained from NASA Worldview application at https://worldview.earthdata.nasa.gov.

Declarations

Competing interests
All authors declare that there are no competing interests.

Author details
[1]State Key Laboratory of Numerical Modelling for Atmospheric Sciences and Geophysical Fluid Dynamics, Institute of Atmospheric Physics, Chinese Academy of Sciences, Beijing 100029, China. [2]University of Chinese Academy of Sciences, Beijing 100049, China. [3]School of Atmospheric Sciences, Sun Yat-Sen University, and Southern Marine Science and Engineering Guangdong Laboratory (Zhuhai), Zhuhai 519082, China. [4] Yangtze Eco-Environment Engineering Research Center, China Three Gorges Corporation, Wuhan 430014, China.

Received: 1 March 2024 Accepted: 10 August 2024
Published online: 22 August 2024

References

Allen JT, Pezza AB, Black MT (2010) Explosive cyclogenesis: a global climatology comparing multiple reanalyses. J Clim 23(24):6468–6484. https://doi.org/10.1175/2010JCLI3437.1
Ashley WS, Black AW (2008) Fatalities associated with nonconvective high-wind events in the United States. J Appl Meteorol Climatol 47(2):717–725. https://doi.org/10.1175/2007JAMC1689.1
Bengtsson L, Hodges KI, Keenlyside N (2009) Will extratropical storms intensify in a warmer climate? J Clim 22(9):2276–2301. https://doi.org/10.1175/2008JCLI2678.1
Brodzik MJ, Billingsley B, Haran T, Raup B, Savoie MH (2012) EASE-grid 2.0: incremental but significant improvements for earth-gridded data sets. ISPRS Int J Geo-Inf 1(1):32–45. https://doi.org/10.3390/ijgi1010032
Carleton AM, Carpenter DA (1990) Satellite climatology of 'polar lows' and broadscale climatic associations for the Southern Hemisphere. Int J Climatol 10(3):219–246. https://doi.org/10.1002/joc.3370100302
Catto JL, Madonna E, Joos H, Rudeva I, Simmonds I (2015) Global relationship between fronts and warm conveyor belts and the impact on extreme precipitation*. J Clim 28(21):8411–8429. https://doi.org/10.1175/JCLI-D-15-0171.1
Clancy R, Bitz CM, Blanchard-Wrigglesworth E, McGraw MC, Cavallo SM (2021) A cyclone-centered perspective on the drivers of asymmetric patterns in the atmosphere and sea ice during Arctic cyclones. Journal of Climate. https://doi.org/10.1175/jcli-d-21-0093.1
Colle BA, Buonaiuto F, Bowman MJ, Wilson RE, Flood R, Hunter R et al (2008) New York city's vulnerability to coastal flooding: storm surge modeling of past cyclones. Bull Am Meteor Soc 89(6):829–842. https://doi.org/10.1175/2007BAMS2401.1
Crawford AD, Serreze MC (2016) Does the summer Arctic frontal zone influence Arctic Ocean cyclone activity? J Clim 29(13):4977–4993. https://doi.org/10.1175/JCLI-D-15-0755.1
Crawford AD, Serreze MC (2017) Projected changes in the arctic frontal zone and summer arctic cyclone activity in the CESM large ensemble. J Clim 30(24):9847–9869. https://doi.org/10.1175/JCLI-D-17-0296.1
Finocchio PM, Doyle JD, Stern DP, Fearon MG (2020) Short-term impacts of arctic summer cyclones on sea ice extent in the marginal ice zone. Geophys Res Lett. https://doi.org/10.1029/2020GL088338
Fogt RL, Marshall GJ (2020) The Southern annular mode: variability, trends, and climate impacts across the Southern Hemisphere. Wires Clim Change 11(4):e652. https://doi.org/10.1002/wcc.652
Fu G, Li PY, Chen LJ, Peng YM, Ni J (2023) Historic and future perspectives of storm and cyclone. Adv Atmos Sci 40:447–463. https://doi.org/10.1007/s00376-022-2184-1
Grieger J, Leckebusch GC, Raible CC, Rudeva I, Simmonds I (2018) Subantarctic cyclones identified by 14 tracking methods, and their role for moisture transports into the continent. Tellus a: Dynamic Meteorology and Oceanography 70(1):1454808. https://doi.org/10.1080/16000870.2018.1454808
Gorodetskaya IV, Tsukernik M, Claes K, Ralph MF, Neff WD, Van Lipzig NPM (2014) The role of atmospheric rivers in anomalous snow accumulation in East Antarctica. Geophys Res Lett 41(17):6199–6206. https://doi.org/10.1002/2014GL060881
Gyakum JR, Anderson JR, Grumm RH, Gruner EL (1989) North Pacific cold-season surface cyclone activity: 1975–1983. Mon Wea Rev 117(6):1141–1155. https://doi.org/10.1175/1520-0493(1989)117%3c1141:NPCSSC%3e2.0.CO;2
Hanley J, Caballero R (2012) Objective identification and tracking of multicentre cyclones in the ERA-Interim reanalysis dataset. Q J R Meteorol Soc 138(664):612–625. https://doi.org/10.1002/qj.948

Hersbach H, Bell B, Berrisford P, Biavati G, Horányi A, Muñoz Sabater J, Nicolas J, Peubey C, Radu R, Rozum I, Schepers D, Simmons A, Soci C, Dee D, Thépaut J-N (2023) ERA5 hourly data on single levels from 1940 to present. Copernicus Climate Change Serv Climate Data Store. https://doi.org/10.24381/cds.adbb2d47

Hersbach H, Bell B, Berrisford P, Hirahara S, Horányi A, Muñoz-Sabater J et al (2020) The ERA5 global reanalysis. Q J R Meteorol Soc 146(730):1999–2049. https://doi.org/10.1002/qj.3803

Hodges KI, Lee RW, Bengtsson L (2011) A comparison of extratropical cyclones in recent reanalyses ERA-Interim, NASA MERRA, NCEP CFSR, and JRA-25. J Clim 24(18):4888–4906. https://doi.org/10.1175/2011JCLI4097.1

Huang B, Liu C, Banzon VF, Freeman E, Graham G, Hankins W et al (2020) NOAA 0.25-degree daily optimum interpolation sea surface temperature (OISST), version 2.1. NOAA Natl Centers Environ Inf. https://doi.org/10.25921/RE9P-PT57

Inatsu M (2009) The neighbor enclosed area tracking algorithm for extratropical wintertime cyclones. Atmos Sci Lett 10:267–272. https://doi.org/10.1002/asl.238

Jena B, Bajish CC, Turner J, Ravichandran M, Anilkumar N, Kshitija S (2022) Record low sea ice extent in the Weddell sea, Antarctica in april/may 2019 driven by intense and explosive polar cyclones. Npj Clim Atmos Sci 5(1):19. https://doi.org/10.1038/s41612-022-00243-9

Lim E-P, Simmonds I (2002) EC development in the Southern Hemisphere and a comparison with northern hemisphere events. Mon Weather Rev 130(9):2188–2209. https://doi.org/10.1175/1520-0493(2002)130%3c2188:ECDITS%3e2.0.CO;2

Meier W, Fetterer F, Windnagel A, Stewart S (2021) NOAA/NSIDC climate data record of passive microwave sea ice concentration, version 4. NSIDC. https://doi.org/10.7265/EFMZ-2T65

Morris WE, Smith PJ (2001) Cyclolysis: a diagnosis of two extratropical cyclones. Mon Weather Rev 129(11):2714–2729. https://doi.org/10.1175/1520-0493(2001)129%3c2714:CADOTE%3e2.0.CO;2

Neu U, Akperov MG, Bellenbaum N, Benestad R, Blender R, Caballero R et al (2013) IMILAST: a community effort to intercompare extratropical cyclone detection and tracking algorithms. Bull Am Meteor Soc 94(4):529–547. https://doi.org/10.1175/BAMS-D-11-00154.1

Pfahl S, Wernli H (2012) Quantifying the relevance of cyclones for precipitation extremes. J Clim 25(19):6770–6780. https://doi.org/10.1175/JCLI-D-11-00705.1

Raible CC, Yoshimori M, Stocker TF, Casty C (2007) Extreme midlatitude cyclones and their implications for precipitation and wind speed extremes in simulations of the maunder minimum versus present day conditions. Clim Dyn 28(4):409–423. https://doi.org/10.1007/s00382-006-0188-7

Reale M, Liberato MLR, Lionello P, Pinto JG, Salon S, Ulbrich S (2019) A global climatology of ECs using a multi-tracking approach. Tellus a 71(1):1611340. https://doi.org/10.1080/16000870.2019.1611340

Reboita MS, da Rocha RP, Ambrizzi T, Gouveia CD (2015) Trend and teleconnection patterns in the climatology of extratropical cyclones over the Southern Hemisphere. Clim Dyn 45(7–8):1929–1944. https://doi.org/10.1007/s00382-014-2447-3

Reboita MS, Crespo NM, Torres JA, Reale M, Porfírio da Rocha R, Giorgi F, Coppola E (2021) Future changes in winter ECs over the Southern Hemisphere domains from the CORDEX-CORE ensemble. Clim Dyn 57(11–12):3303–3322. https://doi.org/10.1007/s00382-021-05867-w

Roebber PJ (1984) Statistical analysis and updated climatology of ECs. Mon Wea Rev 112(8):1577–1589. https://doi.org/10.1175/1520-0493(1984)112%3c1577:SAAUCO%3e2.0.CO;2

Sanders F, Gyakum JR (1980) Synoptic-dynamic climatology of the "bomb." Mon Weather Rev 108(10):1589–1606. https://doi.org/10.1175/1520-0493(1980)108%3c1589:SDCOT%3e2.0.CO;2

Schreiber EAP, Serreze MC (2020) Impacts of synoptic-scale cyclones on Arctic sea-ice concentration: a systematic analysis. Ann Glaciol 61(82):139–153. https://doi.org/10.1017/aog.2020.23

Serreze MC (1995) Climatological aspects of cyclone development and decay in the Arctic. Atmos Ocean 33(1):1–23. https://doi.org/10.1080/07055900.1995.9649522

Sinclair MR (1994) An objective cyclone climatology for the Southern Hemisphere. Mon Weather Rev 122(10):2239–2256. https://doi.org/10.1175/1520-0493(1994)122%3c2239:AOCCFT%3e2.0.CO;2

Sinclair MR (1995) A climatology of cyclogenesis for the Southern Hemisphere. Mon Weather Rev 123(6):1601–1619. https://doi.org/10.1175/1520-0493(1995)123%3c1601:ACOCFT%3e2.0.CO;2

Spensberger C, Reeder MJ, Spengler T, Patterson M (2020) The connection between the southern annular mode and a feature-based perspective on Southern Hemisphere Midlatitude winter variability. J Climate 33:115–129. https://doi.org/10.1175/JCLI-D-19-0224.1

Streten NA, Troup AJ (1973) A synoptic climatology of satellite observed cloud vortices over the Southern Hemisphere. Q J R Meteorol Soc 99(419):56–72. https://doi.org/10.1002/qj.49709941906

Tschudi M, Meier WN, Stewart JS, Fowler C, Maslanik J (2019) Polar Pathfinder Daily 25 km EASE-grid sea ice motion vectors, version 4 [data set]. Boulder, Colorado USA. NASA National Snow and Ice Data Center Distributed Active Archive Center. https://doi.org/10.5067/INAWUWO7QH7B. Accessed 24 Oct 2021.

Vichi M, Eayrs C, Alberello A, Bekker A, Bennetts L, Holland D et al (2019) Effects of an explosive polar cyclone crossing the antarctic marginal ice zone. Geophys Res Lett 46(11):5948–5958. https://doi.org/10.1029/2019GL082457

Wang XL, Feng Y, Compo GP, Swail VR, Zwiers FW, Allan RJ, Sardeshmukh PD (2013) Trends and low frequency variability of extra-tropical cyclone activity in the ensemble of twentieth century reanalysis. Clim Dyn 40(11–12):2775–2800. https://doi.org/10.1007/s00382-012-1450-9

Wille JD, Favier V, Gorodetskaya IV, Agosta C, Kittel C, Beeman JC et al (2021) Antarctic atmospheric river climatology and precipitation impacts. J Geophys Res 126(8):e2020JD033788. https://doi.org/10.1029/2020JD033788

Yoshida A, Asuma Y (2004) Structures and environment of explosively developing extratropical cyclones in the Northwestern Pacific Region. Mon Wea Rev 132(5):1121–1142. https://doi.org/10.1175/1520-0493(2004)132%3c1121:SAEOED%3e2.0.CO;2

Publisher's Note